Propagation Modeling Over Terrain Using the Parabolic Wave Equation

Denis J. Donohue, *Member, IEEE,* and J. R. Kuttler

***Abstract*—We address the numerical solution of the parabolic wave equation over terrain using the Fourier/split-step approach. The method, referred to as a shift map, generalizes that of Beilis and Tappert, who introduced a coordinate transformation technique to flatten the boundary. This technique is extended to a wide-angle form, allowing larger propagation angles with respect to the horizon. A new impedance boundary condition is derived for electromagnetic waves incident on a finitely conducting surface that enables solution of the parabolic wave (PWE) using the previously developed mixed Fourier transform. It is also shown by example that in many cases of interest, the boundary may be approximated by discrete piecewise linear segments without affecting the field solution. A more accurate shift map solution of the PWE for a piecewise linear boundary is, therefore, developed for modeling propagation over digitally sampled terrain data. The shift-map solution is applied to various surface types, including ramps, wedges, curved obstacles, and actual terrain. Where possible, comparisons are made between the numerical solution and an exact analytical form. The examples demonstrate that the shift map performs well for surface slopes as large as 10–15° and discontinuous slope changes on the order of 15–20°. To accommodate a larger range of slopes, it is suggested that the most viable solution for general terrain modeling is a hybrid of the shift map with the well-known terrain masking (knife-edge diffraction) approximation.**

***Index Terms*—Clutter, electromagnetics, parabolic wave equation, propagation, rough boundaries, terrain.**

I. Introduction

FOR many years the parabolic wave equation (PWE) has been widely used to model the propagation of electromagnetic and acoustic waves through inhomogeneous media. Most applications of the PWE consider low-grazing angle or near-horizontal propagation of radar or acoustic waves. In many cases, the horizontal boundary, be it terrain, ocean surface, or ocean bottom, plays a significant role. Numerical solutions of the PWE are largely split into two categories: finite-difference methods and the Fourier/split-step approach [5]. In the finite-difference methods, implementing the appropriate boundary condition is usually straightforward. A disadvantage of finite difference methods, however, is a requirement for fine sampling on the horizontal or range grid, which makes the calculations computationally intensive. Fourier/split-step methods, the subject of this paper, allow for a relatively large range step; however, the boundary condition must be enforced in transform space.

Manuscript received April 28, 1998; revised March 15, 1999. This work was supported by the U.S. Navy AEGIS Shipbuilding Program, PMS-400B.

The authors are with the Applied Physics Laboratory, Johns Hopkins University, Laurel, MD 20723 USA.

Publisher Item Identifier S 0018-926X(00)02620-X.

To accommodate a finitely conducting dielectric (but planar or spherical) boundary in the split-step solution, Kuttler and Dockery [2] developed the mixed Fourier transform (MFT). In addition, several researchers have also considered the problem of large-scale (compared to the wavelength) surface undulations. Tappert and Ngiem-Phu [11] developed a method in which the computational domain is doubled and an "image ocean" or "image atmosphere" is introduced. Rouseff and Ewart [12] subsequently used this method to examine the effect of sea surface and bottom roughness on shallow water acoustic propagation. Because it is an image method, this approach is limited to perfectly conducting or pressure release boundaries. A simple approximation that has also been used [7], [18] is the terrain masking approach. This method, which advances the field as if in free-space and then at each step zeros the field below the altitude of the boundary, is equivalent to representing the boundary by a series of knife-edge diffractors. As a result, all surface reflections are approximated by tip diffraction.

In another approach, Dozier [8] used a local or piecewise conformal mapping to locally flatten the surface while retaining the elliptic form of the wave equation. The parabolic approximation was then applied to the transformed wave equation. Kuttler and Huffaker [6] used a global conformal map to calculate scattering from a sinusoidal boundary. Their results showed excellent agreement with classical Bragg scattering theory based on the Rayleigh plane wave expansion. Beilis and Tappert [9] developed a general coordinate transformation for the narrow angle version of the parabolic wave equation that flattens the undulating surface and retains the PWE. McArthur and Bebbington [22], [23] subsequently investigated tilting or steering the field to counteract the flattening of the surface, which, in part, resembles Beilis and Tappert's approach, but without an explicit coordinate transformation. Barrios [13] tested the actual Beilis/Tappert approach on a variety of sample terrain problems. In another approach to rough surfaces, Rino [14] recently introduced a hybrid PWE/integral equation method that circumvents the numerical difficulties introduced by the rough boundary in the PWE/split-step method. Rino's method also accounts for fine-scale surface roughness, but requires range sampling on the order of the incident wavelength, which is considerably more restrictive than usual for split-step calculations. All of the above-mentioned rough surface studies are limited to perfectly conducting (or acoustically rigid) boundaries and, in most cases, modest surface slopes.

In this paper, we improve on the mapping technique, subsequently referred to as the shift map, developed by Beilis and Tappert [9]. In Section II, we extend the technique to wide angle propagators in the context of the Fourier/split-step method. Sec-

tion III demonstrates that, with sufficiently fine sampling, representing terrain by a piecewise linear surface gives essentially the same propagation results as a continuous representation. Therefore, the wide-angle shift map for piecewise linear terrain can be further improved (Section IV) to handle terrain with larger slopes. The improved shift map is applied in Section V to a model terrain problem and the results are also compared with the geometrical theory of diffraction (GTD) for a perfectly conducting wedge. The slope dependence of the method is examined, and a comparison is made with the terrain masking approach that indicates some important differences.

We also extend the Leontovich impedance boundary condition in such a way that finitely conducting terrain can be solved by the MFT procedure. As discussed above, previous Fourier methods for terrain have generally been restricted to perfectly conducting surfaces. Section VI contains the mathematical derivation of the extended impedance boundary condition, while Section VII compares propagation predictions based on the piecewise linear shift map with impedance boundary to the exact solution for a simple terrain problem. Section VIII describes an application of the new method to an actual terrain sample. Further comparisons are made between horizontal/vertical polarization, and perfect/finite conductivity for a range of frequencies. Section IX summarizes the performance of the improved shift-map technique, its applicability to the general terrain problem, and possible future improvements. The improved shift map will give accurate propagation at angles up to nearly 30°, which means that terrain with slopes up to nearly 15° can be handled. For steeper angles, it is apparently the commutator error in the factorization producing the PWE that limits accuracy.

II. Wide-Angle Shift Map: Theory

In this section, we develop a terrain flattening transformation, subsequently referred to as the shift map, which improves on the mapping developed by Beilis and Tappert [9]. The improved mapping avoids the paraxial approximation, resulting in a self-consistent wide-angle form of the transformed PWE.

The derivation starts with the two-dimensional (2-D) Helmholtz equation

$$\frac{\partial^2\Phi}{\partial u^2}+\frac{\partial^2\Phi}{\partial v^2}+k^2n^2\Phi=0 \tag{1}$$

where

$\Phi(u, v)$	is the scalar field;
$k\ (=2\pi/\lambda)$	is the wavenumber;
n	is the relative index of refraction of the propagating medium;
u, v	are the fixed (unmapped) coordinates as shown in Fig. 1.

In these coordinates, the terrain height is assumed to be given by an equation of the form

$$v=T(u). \tag{2}$$

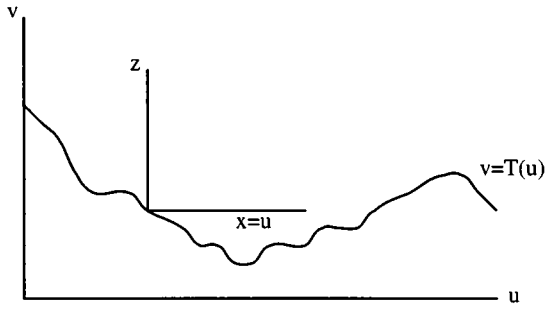

Fig. 1. Illustration of the mapped (x, z) and unmapped (u, v) coordinate systems with a terrain profile.

The terrain flattening transformation originally introduced in [9] is then simply

$$x=u, \qquad z=v-T(u). \tag{3}$$

In the new coordinates, with $\phi(x, z)=\Phi(u, v)$, the Helmholtz equation (1) becomes

$$\left(\frac{\partial}{\partial x}-T'\frac{\partial}{\partial z}\right)^2\phi+\frac{\partial^2\phi}{\partial z^2}+k^2n^2\phi=0 \tag{4}$$

where $T'\equiv dT/dx$.

To eliminate first derivatives in z as required for Fourier transform methods, the function ϕ is replaced with $\psi e^{i\theta}$, where the phase factor $\theta(x, z)$ is yet to be determined. The same substitution was also introduced in [9]. Substituting into (4), we have

$$\left\{\frac{\partial}{\partial x}+i\frac{\partial\theta}{\partial x}-T'\left(\frac{\partial}{\partial z}+i\frac{\partial\theta}{\partial z}\right)\right\}^2\psi + \left\{\frac{\partial}{\partial z}+i\frac{\partial\theta}{\partial z}\right\}^2\psi+k^2n^2\psi=0 \tag{5}$$

where a common factor $e^{i\theta}$ has been dropped from all terms. Equation (5) is now factored as

$$\left[\left\{\frac{\partial}{\partial x}+i\frac{\partial\theta}{\partial x}-T'\left(\frac{\partial}{\partial z}+i\frac{\partial\theta}{\partial z}\right)\right\} + i\sqrt{\left(\frac{\partial}{\partial z}+i\frac{\partial\theta}{\partial z}\right)^2+k^2n^2}\right] \times\left[\left\{\frac{\partial}{\partial x}+i\frac{\partial\theta}{\partial x}-T'\left(\frac{\partial}{\partial z}+i\frac{\partial\theta}{\partial z}\right)\right\} - i\sqrt{\left(\frac{\partial}{\partial z}+i\frac{\partial\theta}{\partial z}\right)^2+k^2n^2}\right]\psi=0. \tag{6}$$

This factorization of (5) introduces an error when the square root operator and the expression in brackets do not commute [15]. This will be the case if the index of refraction depends on the range coordinate x [5]. However, it can be shown that this *commutator error* is small if n is reasonably uniform in range in the original (u, v) coordinates.

As discussed in [15], the first and second factors of (6) correspond to backward and forward propagating waves, respec-

tively. To obtain the parabolic wave equation, we consider forward scattering only by retaining the factor

$$\left[\left\{\frac{\partial}{\partial x}+i\,\frac{\partial\theta}{\partial x}-T'\left(\frac{\partial}{\partial z}+i\,\frac{\partial\theta}{\partial z}\right)\right\} - i\sqrt{\left(\frac{\partial}{\partial z}+i\,\frac{\partial\theta}{\partial z}\right)^2+k^2n^2}\right]\psi=0. \tag{7}$$

In the limit of a flat surface ($T'=0$, $\theta=0$), it can be seen that (7) reduces to

$$\left[\frac{\partial}{\partial x}-i\sqrt{\frac{\partial^2}{\partial z^2}+k^2n^2}\right]\psi=0 \tag{8}$$

which is the well-known starting point for deriving the wide-angle form of the PWE.

To continue with the derivation of the shift-map algorithm, the square root operator in (7) must be put in a form suitable for computation. The operator may be written as

$$k\sqrt{1+x}=k\left(1+\frac{x}{2}-\frac{x^2}{8}+\cdots\right) \tag{9}$$

where

$$x=\frac{1}{k^2}\left(\frac{\partial}{\partial z}+i\,\frac{\partial\theta}{\partial z}\right)^2+(n^2-1)$$

and it is assumed that x is small compared to one. If we retain only the first-order terms, (7) becomes

$$\left\{\frac{\partial}{\partial x}+i\,\frac{\partial\theta}{\partial x}-T'\left(\frac{\partial}{\partial z}+i\,\frac{\partial\theta}{\partial z}\right)\right\}\psi = \frac{i}{2k}\left(\frac{\partial}{\partial z}+i\,\frac{\partial\theta}{\partial z}\right)^2\psi+\frac{ik}{2}(n^2+1)\psi. \tag{10}$$

To obtain the desired form of the parabolic equation, we wish to eliminate terms in $\partial\psi/\partial z$, which may be done by choosing

$$\frac{\partial\theta}{\partial z}=kT' \tag{11}$$

which also implies

$$\frac{\partial^2\theta}{\partial z^2}=0.$$

After substituting (11) and rearranging, (10) becomes

$$\frac{\partial\psi}{\partial x}=\frac{i}{2k}\,\frac{\partial^2\psi}{\partial z^2}+\frac{ik}{2}(n^2+1+T'^2)\psi-i\,\frac{\partial\theta}{\partial x}\,\psi. \tag{12}$$

Some flexibility remains in the choice of θ. From (11), we have

$$\theta(x,z)=kzT'(x)+f(x) \tag{13}$$

where $f(x)$ is an arbitrary function. We could simply choose $\partial\theta/\partial x=0$, as it only affects the overall phase of the field ϕ. However, to put (12) in a particularly simple form, we can take

$$f'(x)=\frac{k}{2}(1+T'^2) \tag{14}$$

which gives us

$$\frac{\partial\psi}{\partial x}=\frac{i}{2k}\,\frac{\partial^2\psi}{\partial z^2}+ik\left(\frac{n^2}{2}-zT''\right)\psi \tag{15}$$

where $T''\equiv d^2T(x)/dx^2$.

Equation (15) is essentially the same PWE derived and used by both Beilis and Tappert [9, eq. (14)] and Barrios [13, eq. (7)]. By retaining only first-order terms in the expansion of the radical of (9), we have recovered the standard form for the *narrow-angle* split-step solution of the PWE. This derivation is more physically intuitive than the one given in [9], where the paraxial approximation is used to derive the PWE before applying the shift-map transformation. We next show that with a higher order (more accurate) expansion of (9), a self-consistent *wide angle* formulation can be obtained.

We return to (7) and incorporate the choice made in (11) to obtain

$$\left\{\left(\frac{\partial}{\partial x}+i\,\frac{\partial\theta}{\partial x}\right)-T'\left(\frac{\partial}{\partial z}+ikT'\right)\right\}\psi = i\sqrt{\frac{\partial^2}{\partial z^2}+2ikT'\,\frac{\partial}{\partial z}-k^2T'^2+k^2n^2}\cdot\psi. \tag{16}$$

To retain higher order terms in the approximation of the radical, we use

$$\sqrt{1+\epsilon+\eta+\zeta}\approx\sqrt{1+\epsilon}+\sqrt{1+\eta}+\tfrac{1}{2}\zeta-1 \tag{17}$$

where

$$\epsilon=\frac{1}{k^2}\,\frac{\partial^2}{\partial z^2}\quad \eta=n^2-1\quad \zeta=\frac{2iT'}{k}\,\frac{\partial}{\partial z}-T'^2.$$

With this choice, (16) can be rearranged to give

$$\frac{\partial\psi}{\partial x}=i\sqrt{k^2+\frac{\partial^2}{\partial z^2}}\cdot\psi+ik\left(n-1+\frac{1}{2}T'^2\right)\psi-i\,\frac{\partial\theta}{\partial x}\,\psi. \tag{18}$$

As in the narrow-angle derivation, (18) can be put in a simpler form by an appropriate choice for $\partial\theta/\partial x$. Taking

$$f'(x)=k(-1+\tfrac{1}{2}T'^2) \tag{19}$$

the wide-angle shift map equation is then

$$\frac{\partial\psi}{\partial x}=i\sqrt{k^2+\frac{\partial^2}{\partial z^2}}\,\psi+ik(n-zT'')\psi. \tag{20}$$

Equation (20) leads directly to the form of the split-step algorithm conjectured by Barrios [13, eq. (8)], who solved the narrow angle equation [essentially (15)] with a *wide-angle* split-step propagator, but cautioned that the wide-angle propagator had not been self-consistently obtained from (15). Because we have employed a similar factoring of the Helmholtz equation, in the limit $T''\to 0$ (flat surface), (20) also reduces to the wide angle form of the PWE first derived in [15].

To obtain some measure of the accuracy of the expansion used in (17), consider the expansion under the assumption of a plane wave propagating along x. Ignoring the effect of the boundary on the plane wave we may therefore set $\partial/\partial z=\partial^2/\partial z^2=0$. To simplify matters further, consider propagation in free-space

$(n = 1)$. Under these conditions, the approximate equality of (17) becomes $\sqrt{1-T'^2} \approx 1-T'^2/2$. The approximation therefore reduces to a first-order binomial expansion of the radical that is obviously inaccurate unless the slope $T' \ll 1$. However, we remark that (20) is only one possible approximation to (16) that may be considered "wide angle." Other choices for the expansion parameters ϵ, η, ζ and function $f(x)$ lead to other slightly better approximate solutions. In Section IV, we will develop an alternative method that is more advantageous for terrain problems and also better approximates the radical while still retaining the required form of the PWE. Section V also includes a numerical comparison of both methods with the GTD on a classical diffraction problem.

III. Wide-Angle Shift Map: Examples

Having derived a wide-angle shift-map PWE, in this section, we examine its application to simple or model terrain problems. Specifically, we consider two surface profiles. The first is a curved and continuously differentiable profile, the sinuson, which has the analytical form

$$T(x) = \begin{cases} h\,\dfrac{1}{2}\left[1+\sin\left(\dfrac{\pi(x-x_1)}{2w}\right)\right], \\ \quad -w < x - x_1 < 3w \\ 0, \quad \text{else} \end{cases} \tag{21}$$

where x_1 simply translates the profile and h, w are the peak height and half width. The second profile, the pyramid, is a particularly simple example of a piecewise linear surface. It has the analytical form

$$T(x) = \begin{cases} h(x-x_1)/w, & x_1 < x < x_1 + w \\ h(x_1+2w-x)/w, & x_1 + w < x < x_1 + 2w \\ 0, & \text{else} \end{cases} \tag{22}$$

which consists of two linear segments on an otherwise flat plane.

One of the advantages of the shift map (20) is that it may be solved by the well-known Fourier/split-step methods developed for flat boundaries. To briefly summarize this method, it can be seen that (20) has a formal solution given by [2]

$$\begin{aligned} \psi(x,z) \cong & \exp\left(\frac{ik}{2}\int_{x_0}^{x} m(x',z)\,dx'\right) \\ & \cdot \exp\left(i\Delta x\sqrt{k^2+\frac{\partial^2}{\partial z^2}}\right) \\ & \times \exp\left(\frac{ik}{2}\int_{x_0}^{x} m(x',z)\,dx'\right)\psi(x_0,z) \end{aligned} \tag{23}$$

where

$$m(x,z) = n(x,z) - zT''(x) \tag{24}$$

contains all of the effects of nonzero slope and curvature of the boundary. We note that substitution of (23) into (20) results in additional error terms on the right-hand side of (20). These kinds of error terms and their effects have been previously analyzed in [2, Appendix].

For now, we assume that the range step integration of the refractivity term is simply approximated by

$$\int_{x_0}^{x} m(x',z)\,dx' = m(x_1,z)\Delta x \tag{25}$$

where $x_1 = (x_0+x)/2$ and $\Delta x = x - x_0$. The suitability of this approximation will obviously be governed by the range step and radius of curvature of the surface profile, an issue that is further discussed below. The key to the Fourier/split-step method is that the middle operator in (23) is implemented in the transform (p) space. This technique [2] results in a numerical solution to (23) that is given by

$$\begin{aligned} \psi(x,z) \cong & e^{i(k/2)m(x_1,z)\Delta x}\mathcal{F}^{-1}\{e^{i\sqrt{k^2-p^2}}\mathcal{F} \\ & \cdot \{e^{i(k/2)m(x_1,z)\Delta x}\psi(x_0,z)\}\}. \end{aligned} \tag{26}$$

The type of transform represented by $\mathcal{F}\{\,\}$ is a function of the boundary condition. For calculations in this section, we assume a Dirichlet boundary condition $(\psi(x, z = 0) = 0)$, which is satisfied by a field having odd symmetry with respect to the boundary. Since we are only interested in the upper half-plane $(z > 0)$, the Fourier sine transform enforces this condition.

Fig. 2 illustrates the application of (26) to the sinuson profile (21). The result is calculated at a frequency of 3 GHz and standard atmosphere refractivity is assumed. The antenna is located 30.5 m above the origin, and a range step of 100 m is used. The result shows strong reflections off of the front face of the sinuson and deep shadowing of the incident field beyond the peak. The shadowing is very nearly geometric; that is, the field strength is significantly reduced within the shadow zone, which follows a roughly geometric form bounded by a line joining the antenna with the peak of the sinuson [16].

To apply the shift-map algorithm over a piecewise linear boundary, one must recall that although (26) propagates the transformed field ψ, the physical field Φ has been replaced by the product $\psi e^{i\theta}$, where θ is given by (12) and (19). In Fig. 2, the term $e^{i\theta}$ was ignored since it only affects the phase of the field Φ. However, over a piecewise linear surface, the function θ is discontinuous across each segment joint, where there is a discontinuous change in slope T' (13). Since the physical field must be continuous in space, the transformed amplitude ψ must have a corresponding phase discontinuity to match the change in $e^{i\theta}$. Specifically, when propagating across the boundary between segments 1 and 2, the field ψ becomes

$$\psi_2(x_{1,2},z) = \psi_1(x_{1,2},z)e^{ikz(T_1'-T_2')} \tag{27}$$

where $x_{1,2}$ is the point of discontinuity and $T_1' - T_2'$ is the corresponding change in slope of the piecewise linear boundary [Fig. 6(a)]. In analogy with phased antenna arrays, the factor $e^{ikz(T_1'-T_2')}$ resembles a "steering" of the incident field or beam within each piecewise column. The beam steering is necessary because the x, z coordinate system, while shifted up and down with the boundary, is simultaneously tilted with respect to the boundary. Note that because the boundary is piecewise linear, the curvature term T'' in (24) is now zero. By going from the continuous shift map to the piecewise linear representation, the continuous integration of the rate of change of slope (23)–(25) is

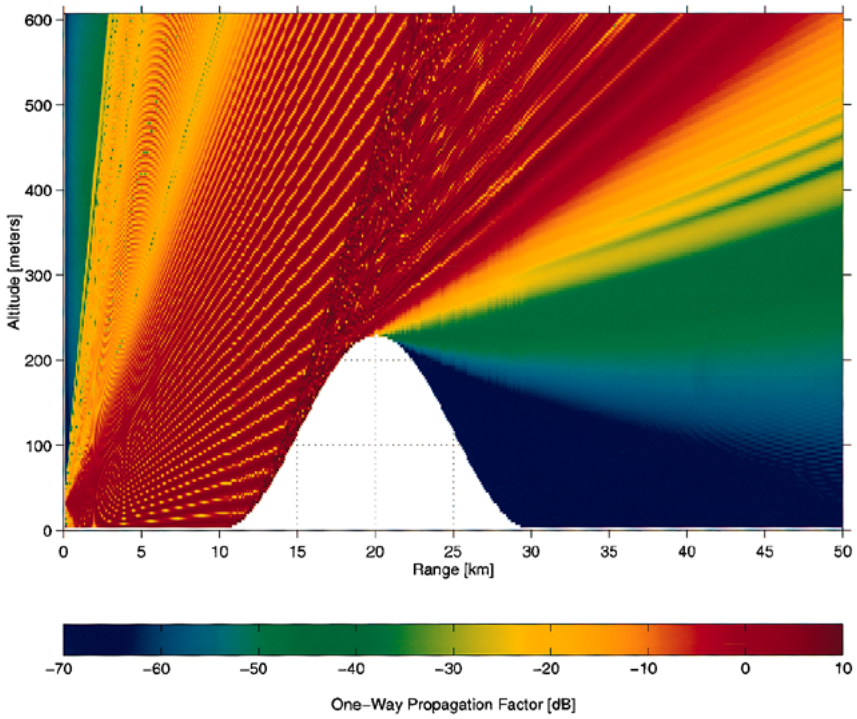

Fig. 2. Propagation over a continuously curved sinuson profile calculated by the wide-angle shift map. A horizontal polarized, 3-GHz source with 3° beamwidth is located 30.5 m above the origin. The surface is perfectly conducting.

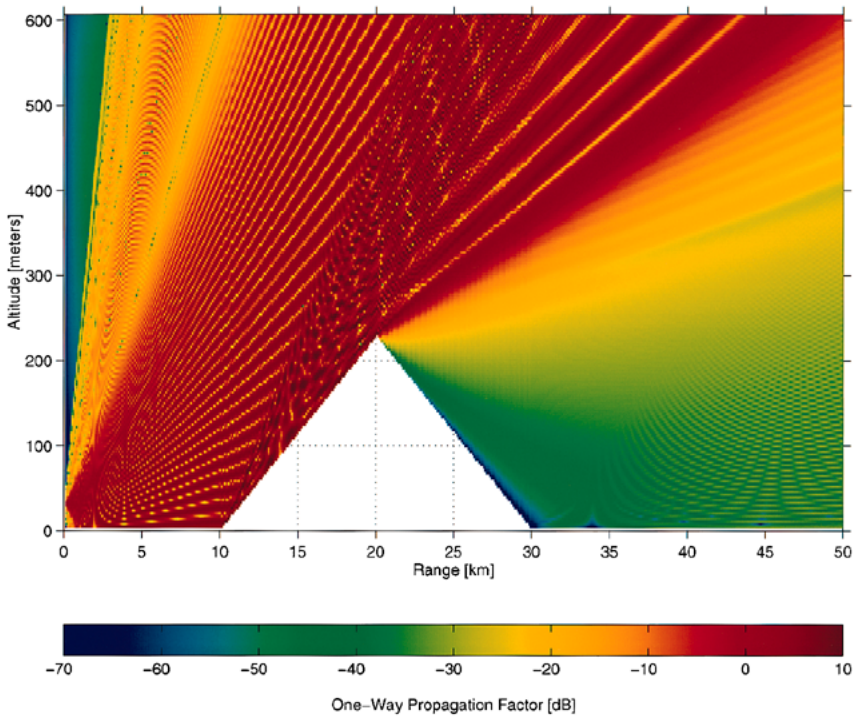

Fig. 3. Same as Fig. 2, but for a piecewise linear wedge or pyramid.

replaced by discrete changes in slope at each segment boundary (27). The relationship between the two approaches is discussed further below.

The application of the piecewise linear shift map to the second profile, the pyramid (22), is illustrated in Fig. 3. Aside from the surface profile, the problem parameters are the same as used in Fig. 2, including the peak height h (229 m), and half-width w (10 km). The most significant difference between Figs. 2 and 3 is the contrast ($\geq$ 25 dB) in the shadowing beyond the peak of the obstacle. There is strong diffraction of the incident field by the vertex of the pyramid, resulting in significantly increased field intensities well into the geometric shadow zone. This result could be critical to radar-terrain applications. Obviously, the shadowing is strongly dependent on both the height and radius

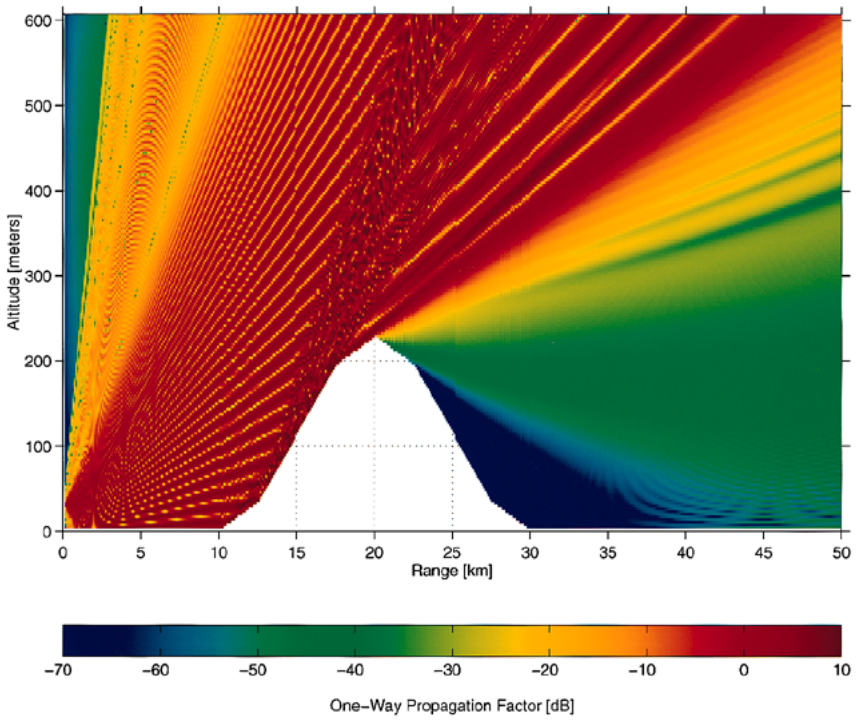

Fig. 4. Same as Fig. 2, except with the sinuson represented by $N = 8$ discrete piecewise linear segments.

of curvature of the terrain. However, when working with sampled terrain data, curvature information may not be available. It is therefore important to know whether accurate propagation predictions can be based solely on terrain elevation samples and, if so, how finely the terrain must be sampled to minimize modeling errors. In the absence of refractive effects $(n = 1)$, GTD may also be used to generate results similar to Figs. 2 and 3, but with limitations on the radius of curvature of the vertex.

To address the terrain sampling issue, the sinuson profile of (21) was also implemented by a piecewise linear representation. Over the range $-w < x - x_1 < 3w$, the profile was broken into N discrete linear segments. A sample calculation for $N = 8$ is shown in Fig. 4. The result differs noticeably from Fig. 2, with the shadowing intermediate to that observed in Figs. 2 and 3. In this case, the piecewise sampling artificially introduces a diffracting wedge that does not appear in the actual (continuous) problem. Fortunately, the result obtained with $N = 20$ samples (not shown) is nearly indistinguishable from the continuous result (Fig. 2). Also of interest is that for the choice of w and Δx, with $N = 20$ the surface segment length of 1 km spans ten range steps. Thus, the 100-m range step used is more than adequately small. Although not conclusive, this result suggests that provided the sampling is sufficiently fine, the piecewise linear representation is a suitable approximation to the continuous shift map. Moreover, the piecewise linear shift map captures vertex or peak diffraction that would be unfeasible to model in the continuously curved case.

It is not surprising that the two representations produce similar results in situations where the terrain lacks sharp discontinuities. To illustrate, consider the problem of Fig. 5, where the continuous map is propagated across a "rounded" corner. From

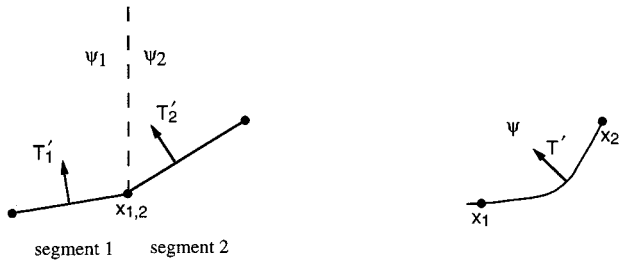

Fig. 5. Geometry for propagating over a changing surface slope for (a) discrete piecewise linear corner and (b) continuously curved sharp corner. The vectors T' represent the local surface slope.

(23) and (24), the slope dependence of the solution at point x_2 is given by

$$\psi(x_2, z) \sim e^{i(k/2)\int_{x_1}^{x_2} m(x', z)\, dx'}\, \psi(x_1, z) \tag{28}$$

where

$$m(x, z) \sim -z\, \frac{d^2 T(x)}{dx^2}.$$

Computing the integral we have

$$\psi(x_2, z) \sim e^{(ikz/2)(T_1' - T_2')}\, \psi_1(x_1, z) \tag{29}$$

which is precisely the "beam-steering" factor of (27). The factor $1/2$ in (29) appears because the operator is split into two in (23). Here we have assumed that the range step is sufficiently small so that the integral of (28) is adequately approximated by the trapezoidal rule in discrete steps. However, in situations where

the radius of curvature is comparable to or smaller than the typical 100-m range step, this may not be the case. In contrast, the piecewise linear shift map will correctly characterize the sharp change in slope (and wedge diffraction) without the fine range step restriction, provided the sharp peak or corner is correctly sampled in the terrain data.

Based on the favorable results obtained with the piecewise linear shift map and the fact that in actual terrain problems one works from discretely sampled data, the remainder of this paper further develops the piecewise linear representation. The results shown in this section are without independent validation. However, the wide-angle shift map, (20) with (27), and the improved piecewise linear representation (Section IV) are all compared with GTD calculations in Section V.

IV. Piecewise Linear Shift Map: Theory

Section III demonstrated the advantage and practical utility of a piecewise linear representation of the shift map. Given that over each linear segment the slope T' is constant and curvature T'' is zero, it is now shown that the algorithm developed in Section II, specifically the operator expansion of (17), can be further improved.

In place of (12), we write the phase function θ as

$$\theta(x,z) = k_0 z T' + f(x) \tag{30}$$

where k_0 is a constant whose value will be determined presently. Substituting into (7) and rearranging gives

$$\left\{\frac{\partial}{\partial x} + if' - T'\left(\frac{\partial}{\partial z} + ik_0T'\right)\right\}\psi = i\sqrt{\frac{\partial^2}{\partial z^2} + 2ik_0T'\frac{\partial}{\partial z} - k_0^2T'^2 + k^2n^2}\cdot\psi \tag{31}$$

which resembles (16). Now the radical may be written as

$$\sqrt{\frac{\partial^2}{\partial z^2} + 2ik_0T'\frac{\partial}{\partial z} - k_0^2T'^2 + k^2n^2} = K\sqrt{1+\epsilon+\eta+\zeta} \tag{32}$$

where

$$K^2 = k^2 - k_0^2T'^2 \qquad \epsilon = \frac{1}{K^2}\frac{\partial^2}{\partial z^2}$$
$$\eta = \frac{k^2}{K^2}(n^2-1) \qquad \zeta = \frac{2ik_0T'}{K^2}\frac{\partial}{\partial z}.$$

Using (17) to expand the radical, the right-hand side of (31) becomes

$$i\left[\sqrt{K^2 + \frac{\partial^2}{\partial z^2}} + \sqrt{k^2n^2 - k_0^2T'^2} + \frac{ik_0T'}{K}\frac{\partial}{\partial z} - K\right]\psi. \tag{33}$$

Getting the $\partial\psi/\partial z$ terms to cancel from (31) requires that $k_0 = K$ or

$$k_0 = \frac{k}{\sqrt{1+T'^2}}. \tag{34}$$

If we then rearrange and choose

$$f'(x) = k_0(-1+T'^2) \tag{35}$$

and substitute (34) and (35) into (31) and (33), we obtain the equation

$$\frac{\partial\psi}{\partial x} = i\sqrt{\frac{k^2}{1+T'^2} + \frac{\partial^2}{\partial z^2}}\cdot\psi + ik\sqrt{\frac{n^2-T'^2}{1+T'^2}}\cdot\psi. \tag{36}$$

Equation (36) is an improved piecewise linear version of the wide-angle shift-map algorithm [(20), for example]. In particular, the expansion of (32) takes advantage of the fact that slope T' is a known constant over the piecewise linear segment. Thus, by moving the term $k_0^2T'^2$ into the constant K that is factored outside of the radical, the magnitude of the expansion variable ζ is reduced relative to the choice made earlier in (17). For example, to compare the two expansions more directly, consider the situation posed in Section II, where the expansion of (17) reduces to $\sqrt{1-T'^2} \approx 1 - T'^2/2$. Using the same expansion as in (17) but with the choice of ϵ, η, ζ shown in (32), for the same plane wave propagation along x and for $n = 1$, the variable ζ becomes zero and the expansion is exact. Specific numerical tests of these two expansions are also shown in the following section.

Comparing (36) to (20), the previous wide-angle result, we find that the wavenumber k in the p-space propagator of (20) is replaced by $k/\sqrt{1+T'^2}$. If we write

$$T' = \tan\beta \tag{37}$$

where β is the angle that the local terrain slope makes with the horizontal, then the effective wavenumber in the piecewise linear version may also be written as $k\cos\beta$. This contraction of the wavenumber (or stretching of the wavelength) is due to the fact that the tilting of the coordinate system by an angle β relative to the surface has locally contracted the horizontal range step. Given (37), the piecewise linear shift map (36) may also be written as

$$\frac{\partial\psi}{\partial x} = i\sqrt{k^2\cos^2\beta + \frac{\partial^2}{\partial z^2}}\cdot\psi + ik\sqrt{n^2 - \sin^2\beta}\cdot\psi. \tag{38}$$

As a result of (30) and (34), the phase discontinuity when propagating across the boundary between linear segments 1 and 2 is now accounted for by

$$\psi_2(x_{1,2},z) = \psi_1(x_{1,2},z)e^{ikz[(T_1'/1+T_1'^2)-(T_2'/1+T_2'^2)]} = \psi_1(x_{1,2},z)e^{ikz[\sin\beta_1 - \sin\beta_2]} \tag{39}$$

in place of (27). Thus, the phase term can be exactly interpreted as a steering factor on the phased array $\psi(x_{1,2}, jdz), j = 0, 1, \cdots, N$. Unlike the previous wide-angle result (27), the angle through which the array is steered is now precisely the physical angle representing the difference in tilt of the linear segments on either side of the vertex $x_{1,2}$. Note that when steering a phased array, there is a condition on the

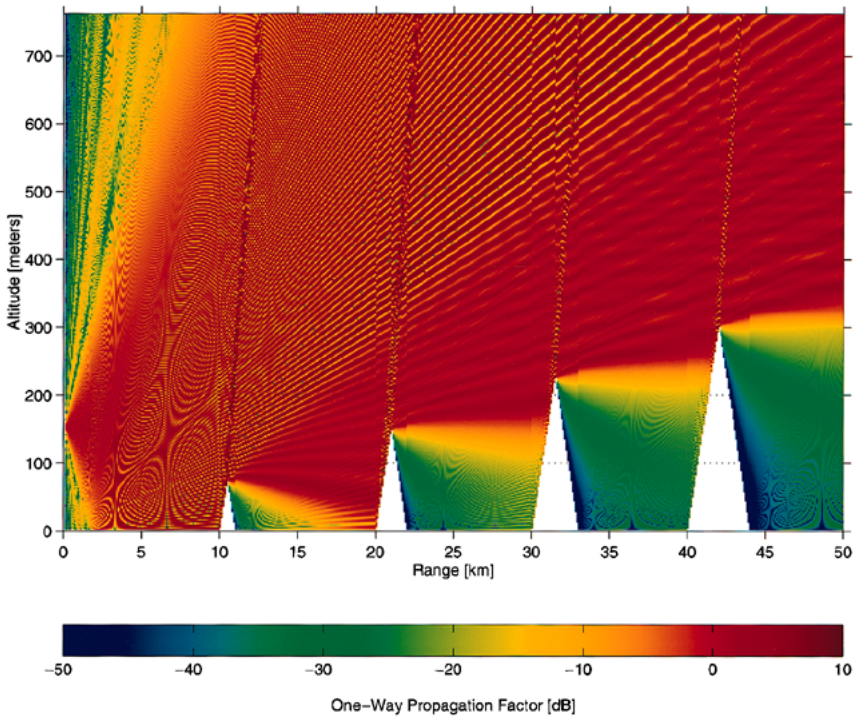

Fig. 6. Propagation over a model terrain profile calculated by the piecewise linear wide-angle shift map. The pyramid slopes are each 8.67°. A horizontal polarized 3-GHz source with 3° beamwidth is located 152 m above the origin. The surface is perfectly conducting.

array spacing to avoid grating lobes. The condition, discussed in [17, ch. 6, p. 545], is

$$dz < \frac{2\pi}{k(1+\sin\theta_M)} \tag{40}$$

where θ_M is the largest angle through which the array is steered. Interestingly, this is a more severe condition on the vertical mesh spacing than is imposed by the sampling condition, which only requires that

$$dz < \frac{\pi}{k\sin\theta_M}. \tag{41}$$

The mathematical formalism of the shift map, starting from the coordinate transformation of Beilis and Tappert [9], has led to (38) and (39). These equations can now be physically interpreted as a tilting or steering of the field array, contraction of the wavenumber in the locally tilted coordinate frame, and a slope-dependent modification of the index of refraction as shown in (38). This may be contrasted with the approach of McArthur and Bebbington [22], who simply tilted the field array without the additional corrections to the wavenumber and index of refraction.

V. Piecewise Linear Shift Map: Examples

We next demonstrate the application of the improved piecewise linear shift map to model terrain problems. The first problem consists of a series of four pyramid shapes with ascending peak heights. The pyramid slopes are fixed to $\pm 8.67°$, with peak heights of 76, 152, 229, and 305 m, respectively. A 3-GHz source with 3° beamwidth is located 152 m above the terrain. The source is propagated according to (38) with a Dirichlet boundary condition (perfect conductivity–horizontal polarization). As in Section III, standard atmosphere refractivity is assumed. The result is shown in Fig. 6. The sharp peak diffraction identified in Section III is again observed over each of the obstacles. Because of the changing angle of incidence relative to the vertex, the shadow region behind each obstacle is progressively deeper for the larger peaks. A very slight distortion of the field is observed near the vertices. This distortion is apparently a limitation of the shift-map method whose severity is directly related to the discontinuous change in surface slope. For example, the change in slope at each vertex or the angle through which the field is steered relative to the surface is 17.33° for each of the peaks shown in Fig. 6. For smaller changes in slope (Fig. 3, for example) the distortion is imperceptible. For changes on the order of 25°, the algorithm clearly begins to break down.

As discussed in the previous sections, there are three sources of error in these calculations. The first source is the commutator error that is made when factoring the wave equation (5). Although the operators in (5) are written in terms of the transformed (x, z) coordinates, the equation is essentially factored in the original (u, v) coordinates. Thus, if the refractive index n is reasonably uniform in range, the commutator error will be small. The second source of error is the inherent error terms that arise from the split-step solution (23) of the parabolic wave equation. Finally, additional errors arise from the expansion of the square root operator in the transformed coordinates. Although the accuracy of this expansion is explicitly slope dependent, the choice of expansion variables made in (32) for the piecewise linear representation of the shift map was shown to be optimal. It is important to recall that the expansion used must retain the parabolic form of the wave equation.

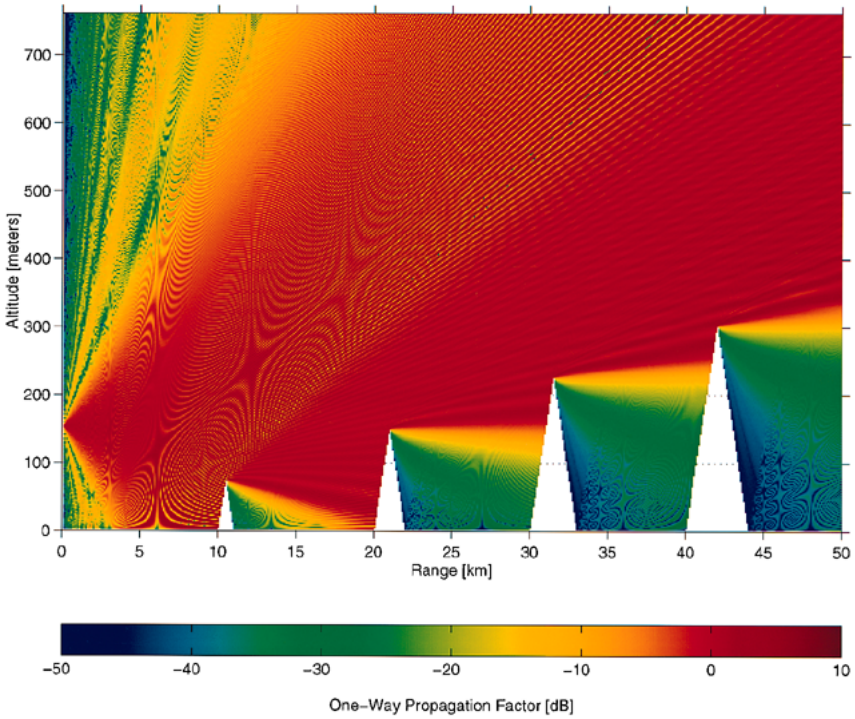

Fig. 7. Same as Fig. 6 but calculated by the terrain masking approximation.

It is interesting to compare the result of Fig. 6 to a simple approximation, known as terrain masking, that has been used previously for propagation over terrain. As mentioned in the introduction, this method is equivalent to representing the boundary by a series of knife-edge diffractors. Fig. 7 shows the terrain masking approach applied to the four-peak problem. Qualitatively, the results of Figs. 6 and 7 appear quite similar. However, significant differences are found in the surface reflections and, to a lesser extent, the degree of shadowing behind the obstacles. While Fig. 6 shows strong reflections from the front faces, through their interference with the direct wave (above each peak) the reflections in Fig. 7 are very weak. Furthermore, while the shift-map approach may also be developed for finitely conducting boundaries (Section VI), terrain masking is limited to perfect conductivity. Therefore, in situations where surface reflections are important, the shift map is the preferred method.

It can also be seen by careful inspection of Figs. 6 and 7 that the shift map predicts deeper shadow regions behind each of the obstacles. To examine the shadowing more carefully and also to provide a comparative measure of the accuracy of the various approaches discussed here, we next consider the classical problem of diffraction by a perfectly conducting wedge. The problem, shown in Fig. 8(a), is chosen because of the availability of a GTD solution. Referring to the GTD formalism of references [20] and [21], a plane wave of horizontal (TE) polarization is assumed to be incident on the wedge at angle ϕ' relative to the front face. For a given observation angle ϕ and observation distance s from the vertex, the incident and diffracted fields are then given by

$$E^{\text{inc}}(s,\phi) = e^{iks\cos(\phi-\phi')}$$
$$E^{d}(s,\phi) = E^{\text{inc}}(Q_e)D^{k}(\phi,\phi',\pi/2,m)\,\frac{e^{-iks}}{\sqrt{s}} \tag{42}$$

where (43), shown at the bottom of the page, $E^{\text{inc}}(Q_e)$ is the incident field at the vertex, and $m = (2\pi - \alpha)/\pi$, where α is the internal wedge angle.

The GTD solution for the diffracted field is to be compared with PWE solutions for a wedge of base $b = 8000$ m and height $h = 760$ m [Fig. 8(b)]. For these values, the slope relative to the lower boundary is $\beta = \pm 10.79°$ or an internal wedge angle $\alpha = \pi - 2\beta = 158.43°$. To reproduce the problem geometry as closely as possible for PWE solutions, the finite wedge is placed 10 km downrange from a 3-GHz source located 152 m above the lower boundary. To model the wedge in free-space, the lower boundary for $x \le 10$ km and $x \ge 18$ km is treated as perfectly absorbing. The absorbing or free-space boundary is eliminated from the propagation step (26) by the following choice of transforms. The sine transform and its inverse enforce a Dirichlet boundary condition ($\psi = 0$ on S), which is equiv-

$$D^{k} = \frac{-e^{-i\pi/4}\sin(\pi/m)}{2m\sqrt{2\pi k}}\left[\frac{1}{\cos(\pi/m)-\cos\left(\dfrac{\phi-\phi'}{m}\right)} - \frac{1}{\cos(\pi/m)-\cos\left(\dfrac{\phi+\phi'}{m}\right)}\right] \tag{43}$$

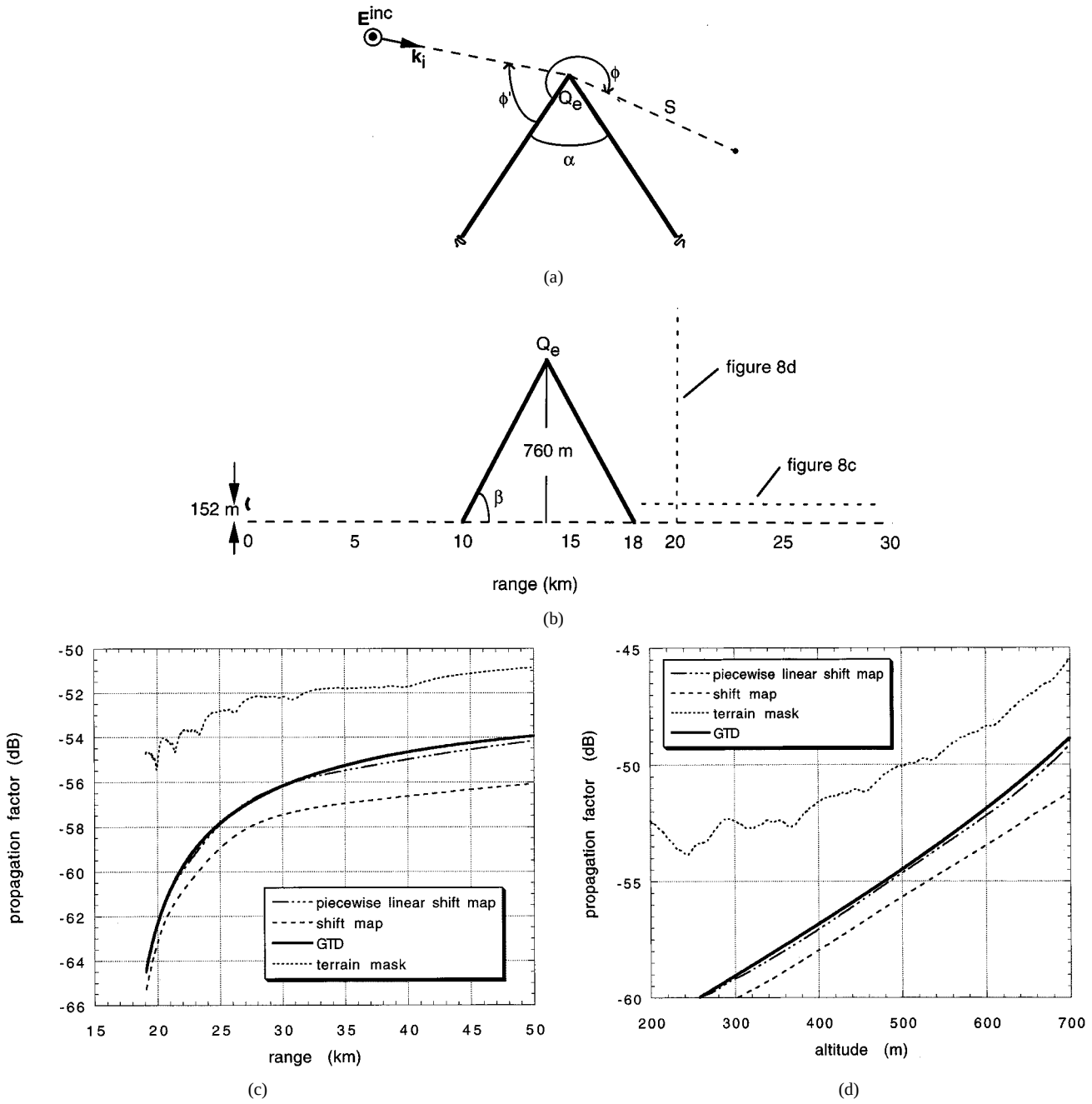

Fig. 8. Propagation over a perfectly conducting wedge. (a) Coordinate system and geometry for GTD solution. (b) Geometry for PWE numerical solution. Dashed line indicates perfectly absorbing (nonreflecting) boundary. (c) Relative intensity calculated by the shift map, piecewise linear shift map, and terrain mask methods compared with GTD solution. Solution is plotted as a function of range at 152 m altitude as shown in (b) and (d). Relative intensity plotted as a function of altitude at 20 km range, as shown in (b).

alent to having a negative image source below the boundary or, in the upper half-space, odd reflections from the boundary. The cosine transform and its inverse is equivalent to a positive image source below the boundary or even reflections from the boundary. The sum of the cosine and sine transform is therefore equivalent to no image source and no reflections. Thus, the source propagates as if no boundary is present. Over the range 10 km $\leq x \leq$ 18 km, the surface of the wedge is perfectly conducting, thus a sine transform (Dirichlet boundary) is used. In addition, the PWE solutions are generated under free-space conditions $(n = 1)$. For a direct comparison of the GTD and PWE solutions, the numerical value of the field $E^{\text{inc}}(Q_e)$ at the vertex is taken directly from the PWE solution and used to normalize the GTD results as shown in (42). As a result, no free parameters are assumed for either GTD or PWE solutions.

Fig. 8(c) compares the propagation factor from each of the various methods as a function of range behind the wedge. The result is generated at a fixed altitude of 152 m, as shown in Fig. 8(b). The GTD solution and piecewise linear shift map (38) agree to within 0.25 dB throughout the entire range of the calculation. The original wide-angle form of the shift map (20) differs from the GTD solution by as much as 2 dB. We remark that the same calculations have been repeated for smaller slopes (β) and, as expected, both versions of the shift-map converge to

the GTD solution in this limit. For comparison, the terrain mask solution is also shown in Fig. 8(c). Consistent with the observations of Figs. 6 and 7, the terrain mask solution overestimates the penetration of the field into the shadowed regions. In particular, within the deep shadow zone (19 km $\leq x \leq$ 21 km), the differences are as large as 6–7 dB.

Fig. 8(d) examines the same calculations as a function of altitude at a fixed range of 20 km (immediately behind the wedge). Again, the GTD solution and piecewise linear shift map are nearly indistinguishable. As in Fig. 8(c), the original wide-angle shift map solution differs from the GTD result by 1–2 dB. The terrain mask solution again overestimates the field throughout. Deep into the shadow zone (near the surface, $z = 0$) the terrain mask error approaches 10 dB. Fig. 8 therefore demonstrates the improved accuracy of the piecewise linear form of the wide-angle shift map as well as the errors encountered (particularly in the shadow zone) when using the simple terrain mask (knife-edge diffraction) approximation. As mentioned in Section III, accurate field strength predictions in the shadow zone are potentially of great interest to radar applications. For example, the shadowing impacts the detectability of low-flying targets, as well as the clutter return from the shadowed terrain.

VI. Piecewise Linear Shift Map with Finitely Conducting Boundaries

Section III briefly described the Fourier/split-step solution to the PWE of the form of (38), the improved piecewise linear shift map. As mentioned, the type of transform that is used depends on the boundary condition. Kuttler and Dockery [2] developed the MFT to propagate an equation of the form of (38) over an impedance-type boundary. To apply the MFT in x, z space requires an approximate relation connecting $\partial\psi/\partial z$ and ψ on the boundary $(z = 0)$. Since the z coordinate is in general oblique, the z derivative must be expressed in terms of normal and tangential derivatives with respect to the boundary. The standard Leontovich impedance boundary condition [4], [24] provides the required relation on the normal derivative but does not involve the tangential derivative [24]. Strictly speaking, the ratio of the field to its oblique derivative is not an impedance condition since it does not follow from a relationship between electric and magnetic fields. However, we can derive the required relationship from first principles as an extension of the standard Leontovich impedance boundary condition.

Given the substitution $\psi = e^{i\theta}\phi$, we have

$$\begin{aligned}\frac{\partial\psi}{\partial z} &= e^{i\theta}\left(\frac{\partial\phi}{\partial z} - i\,\frac{\partial\theta}{\partial z}\,\phi\right)\\ &= e^{i\theta}\left(\frac{\partial\phi}{\partial z} - \frac{ikT'}{\sqrt{1+T'^2}}\,\phi\right)\end{aligned} \tag{44}$$

where (30) is used for the function $\theta(x, z)$. According to the coordinate transformation of Section II, $\phi(x, z) = \Phi(u, v)$, and $\partial\phi/\partial z = \partial\Phi/\partial v$. Therefore, (44) gives the required relation on the z derivative, provided we can find the relationship between Φ and its vertical derivative $\partial\Phi/\partial v$ on the boundary. As in the derivation of the standard Leontovich boundary condition, we suppose that Φ can be locally approximated by an incident and reflected plane wave in the vicinity of the boundary point. The linear segment of terrain in u, v space is given by $v = u\tan\beta$, and the incident plane wave is

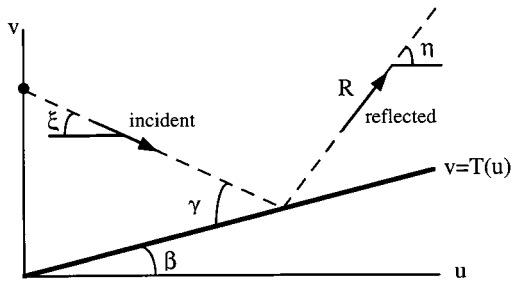

Fig. 9. Geometry for deriving an extended Leontovich impedance boundary condition for the shift map.

$$e^{ik(u\,\cos\xi - v\sin\xi)} \tag{45}$$

where ξ is the angle that the direction of propagation of the plane wave makes with the horizontal. The propagation direction then intersects the boundary segment at the grazing angle $\gamma = \xi + \beta$ (Fig. 9). Similarly, the reflected wave is

$$Re^{ik(u\cos\eta + v\sin\eta)} \tag{46}$$

where R is the polarization-dependent Fresnel reflection coefficient, and $\eta = \gamma + \beta$. Differentiating the total (incident + reflected) field with respect to v, we have

$$\frac{\partial\Phi}{\partial v} = -ik\sin\xi e^{ik(u\cos\xi - v\sin\xi)} + Rik\sin\eta e^{ik(u\cos\eta + v\sin\eta)}. \tag{47}$$

On the boundary $v = u\tan\beta$, it can be shown that

$$u\cos\xi - v\sin\xi = u\cos\eta + v\sin\eta = u\,\frac{\cos\gamma}{\cos\beta}. \tag{48}$$

Combining (45)–(48), we obtain the relation between Φ and its vertical derivative in u, v space

$$\frac{\partial\Phi}{\partial v} = -ik\frac{\sin\xi - R\sin\eta}{1+R}\,\Phi, \quad \text{on } v = u\tan\beta. \tag{49}$$

Equation (49) is now substituted into (44) to obtain

$$\frac{\partial\psi}{\partial z} = -ik\left(\frac{\sin\xi - R\sin\eta}{1+R} + \sin\beta\right)\psi, \quad \text{on } z = 0 \tag{50}$$

where we have used the above-noted relationships between the fields ψ, ϕ, Φ, and their vertical derivatives. Finally, in terms of the angles γ and β, (50) becomes

$$\frac{\partial\psi}{\partial z} + ik\cos\beta\left[\sin\gamma\left(\frac{1-R}{1+R}\right) + \tan\beta(1-\cos\gamma)\right]\psi \quad \text{on } z = 0 \tag{51}$$

the impedance boundary condition for the piecewise linear shift map. In the limit of zero slope $(\beta = 0)$, this again reduces to the standard Leontovich impedance boundary condition

$$\frac{\partial\psi}{\partial z} + \alpha\psi = 0, \qquad \text{on } z = 0. \tag{52}$$

With the boundary condition (51), the previously-developed MFT [2], [3] can be used to propagate the shift map PWE, (38), over an impedance boundary. In place of the usual Leontovich coefficient

$$\alpha = ik \sin\gamma \left(\frac{1-R}{1+R}\right) \tag{53}$$

we have

$$\bar{\alpha} = \cos\beta[\alpha + \tan\beta(1-\cos\gamma)]. \tag{54}$$

This result is very straightforward, but requires knowledge of the grazing angle at each range step. Several methods for grazing angle estimation [3], [18] have been developed, including one based on the spectral estimator MUSIC [19]. Because the estimated grazing angle is a numerical approximation based on the assumption of a single, dominant plane wave incidence angle, an additional source of error is introduced into the calculation. The approximation of the fields as locally plane waves in the vicinity of the boundary can break down under certain types of strong refractive ducting conditions. In [3], it is shown that a single dominant grazing angle may still be determined using a combination of spectral estimation and geometric optics. The grazing angle is also required to model the effect of fine scale terrain roughness on the reflection.

VII. Finitely Conducting Boundaries: Examples

This section compares the solution generated by the piecewise linear shift map (38) with the impedance boundary condition (51) to an analytical solution of a simple terrain problem. In Section V, the shift map was compared with the GTD solution for the perfectly conducting wedge. Here, the surface impedance is included as well, and the slope dependence of the solution is explicitly tested with a suitable benchmark problem. The problem consists of a point source radiator $(\psi(x=0,z) = \delta(z-z_s))$ in vacuum $(n(x,z)=1)$ with a semi-infinite planar surface originating at the point $x = x_1$ and having slope β. Mathematically, the surface segment is given by

$$T(x) = (x-x_1)\tan\beta \qquad x \geq x_1. \tag{55}$$

For $x < x_1$, the problem is unbounded. This is done to eliminate multiple reflections from the surface and thereby permit an analytical solution. For PWE simulations, the boundary is eliminated from the propagation step by a combination of cosine and sine transforms as discussed in Section V.

The analytical solution for the test problem is straightforward to obtain when the Norton ground wave term is neglected. This approximation is justified on the basis of numerical comparisons in the examples to follow. For comparison to the piecewise linear shift map PWE, we consider only the magnitude of the field evaluated *on* the surface of the ramp $(z=0)$. In addition, we consider only the propagation factor, or the magnitude of the field relative to that obtained at the same point in free-space without the boundary present. Given that no multiple reflections occur, the propagation factor (in decibels) for the test problem neglecting the ground wave term is given by $20\log_{10}(|1+R|)$ where R is the complex reflection coefficient at the surface

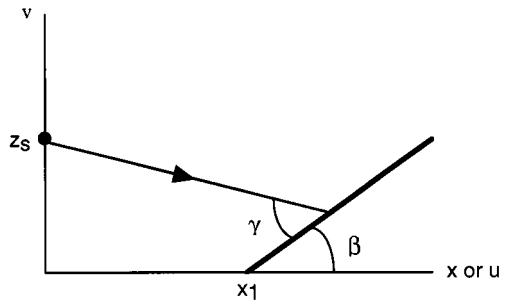

Fig. 10. Sample terrain problem used to test the extended impedance boundary condition. To avoid multiple reflections, the boundary originates at the point $u = x_1, v = 0$.

point. Note that in the PWE solution, the reflected field is included implicitly through the impedance boundary condition. Comparing the PWE solution to this analytical formula directly on the surface gives a strong test of the coordinate-transformed boundary condition approach. For the analytical solution to the test problem, the reflection coefficient [1] is a function of both the complex dielectric constant of the surface (values of $\epsilon_1 = 80$ and $\sigma = 4$ mho/m are used here) and the grazing angle (γ) of the incident field. Since we have chosen a point source radiator in vacuum, the grazing angle is simply the geometric angle intercepted by a ray from the source point. From Fig. 10, an analytical expression for the grazing angle is

$$\gamma = \beta + \tan^{-1}\left(\frac{z_s - T(x)}{x}\right) \qquad x > x_1. \tag{56}$$

One advantage of this simple problem is that values of the grazing angle vary from very large near the source to vanishingly small far from the source. Our objective is to demonstrate that the MFT correctly reflects the physical field when applied to the transformed PWE and boundary condition and that the result holds over a range of surface slopes $(\tan\beta)$ and grazing angles.

Fig. 11 compares the MFT result to the analytical solution for a ramp originating at $x_1 = 0.2$ nautical miles (nmi). The source is located at $z_s = 1000$ ft and radiates at 50 MHz. The solution for $0 \leq x \leq x_1$ is 0 dB since the field propagates in free-space. The solution for $\beta = 0$ corresponds to an untilted surface, which does not require the shift map algorithm. The excellent agreement between the analytical and PWE solutions for this case justifies omitting the Norton ground wave term in the analytical solution. For $-10^\circ \leq \beta \leq 10^\circ$, the agreement between exact and PWE solution is very good. For larger angles, the agreement is not as good, though still reasonable. The results for negative slope are somewhat better, apparently resulting from the much smaller local grazing angles than for the positive slope (for this problem, a slope of $\beta = -39.4^\circ$ would give zero grazing angle.)

While Fig. 11 provides a test of the piecewise linear shift map and impedance boundary condition, actual terrain problems typically involve sudden changes in slope at large distances from the source (with correspondingly small grazing angles). The change in slope causes a discontinuity in the reflection coefficient and should result in a discontinuous jump in the field magnitude on the surface. The discontinuity is next examined for a ramp originating at $x_1 = 10$ nmi (Fig. 12). The grazing

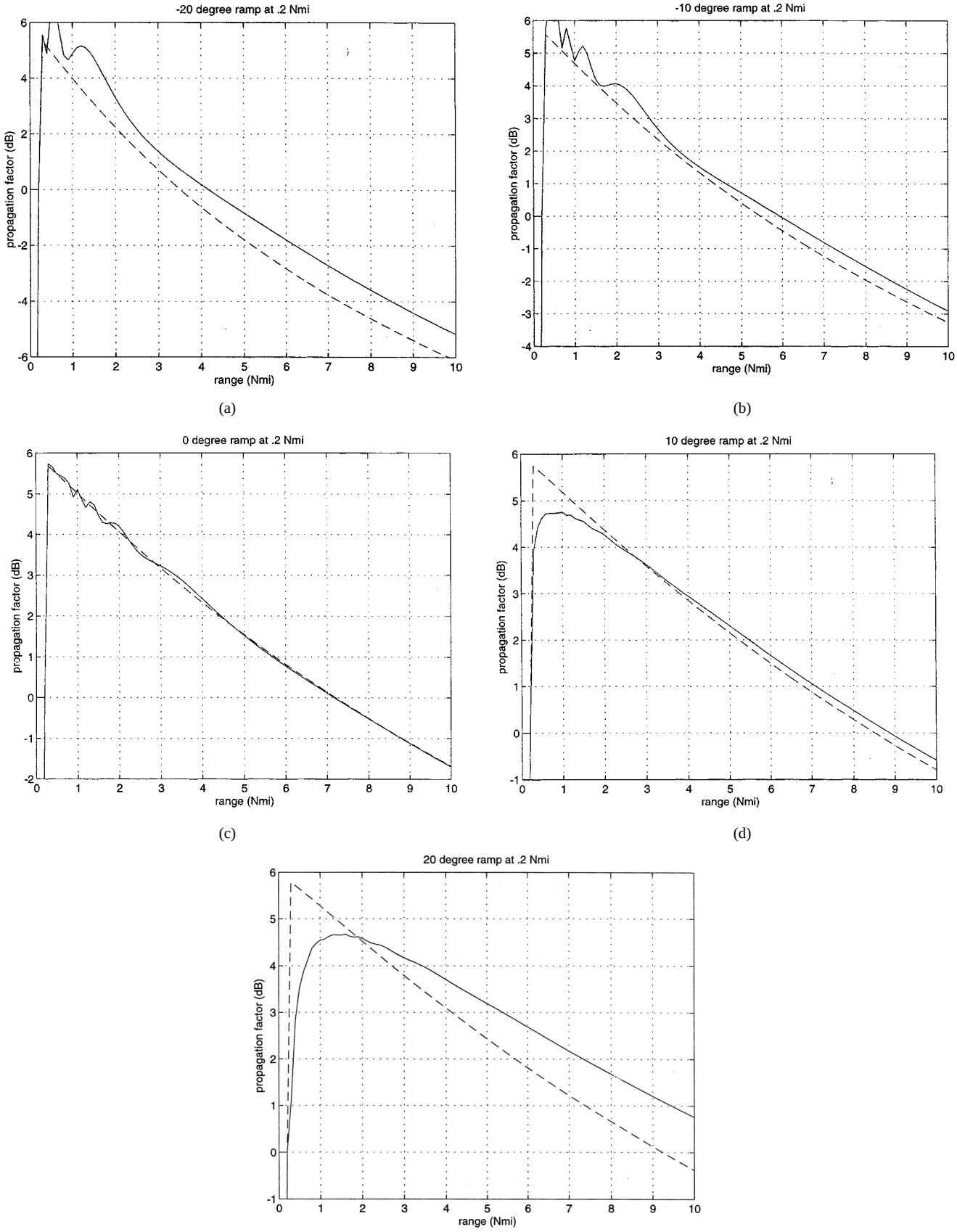

Fig. 11. Comparison of the shift map with impedance boundary condition (solid line) to the exact solution (dotted line) for the problem shown in Fig. 10. The point x_1 is located at 0.2 nmi. Panels (a)–(e) are for slope angles (β) of -20, -10, 0°, 10°, 20, respectively.

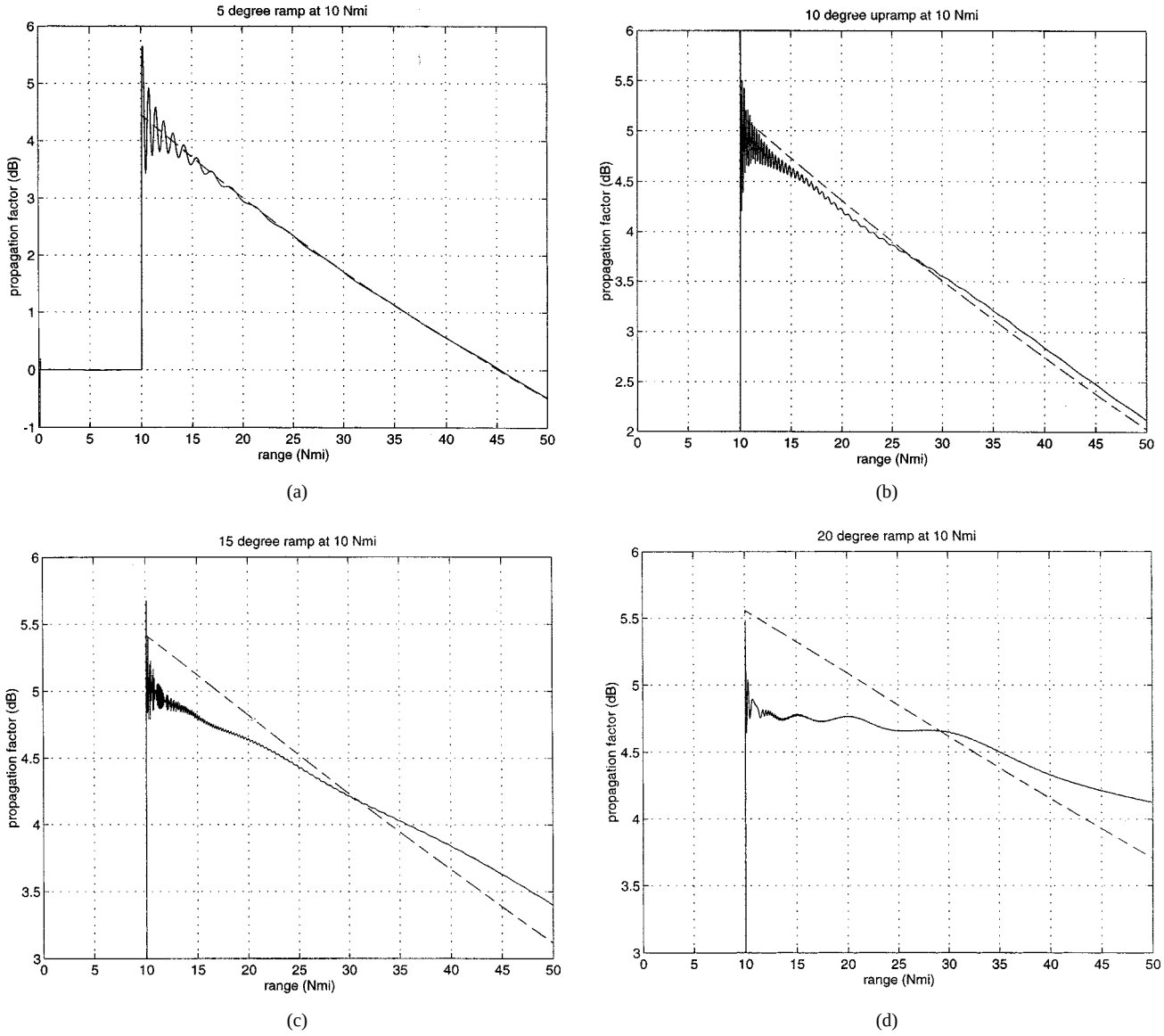

Fig. 12. Comparison of the shift map with impedance boundary condition (solid line) to the exact solution (dotted line) for the problem shown in Fig. 10. The point x_1 is located at 10.0 nmi. Panels (a)–(d) are for slope angles (β) of 5°, 10°, 15°, 20°, respectively.

angle at this distance is $0.94°$ for an untilted surface. We therefore consider only positive slopes since negative slopes larger than $-0.94°$ will be in shadow from the source and the analytical solution discussed above is no longer valid. As shown in Fig. 12, the jump in the field is well reproduced, and it correctly follows the analytical solution as a function of surface slope. As expected, the results for $\beta \leq 10°$ are markedly better, and the accuracy degrades for large angles. The slope-dependent error is discussed at length in Sections IV and V. It is shown that the expansion of (17) can be made optimal in the piecewise linear case by the choice made in (32). Although this expansion is exact in certain limits, in the general case there will be an increasing error with surface slope that is unavoidable. Based on numerical experiments of this type, an upper limit for positive surface slopes is therefore observed to be on the order of $15°$ to $20°$ for small grazing angles. In the near field of the source, where much larger grazing angles may occur (Fig. 10), the slope limit will be correspondingly smaller.

VIII. Propagation over Sampled Terrain

In the previous sections, a model was developed for propagation over finitely conducting boundaries having a relatively wide range of surface slopes. To conclude the paper, we demonstrate an application of the model to an actual terrain profile taken from National Imagery and Mapping Agency's digital terrain elevation data (DTED). The example, shown in Fig. 13(a), is mountainous terrain climbing to an elevation greater than 6000 ft. The surface slopes for this profile, shown in Fig. 13(b), exceed the range of validity of the wide angle shift map as established in the previous sections. To make the profile suitable for propagation predictions, a smoothing algorithm is applied. The smoothed realization of the surface is shown in Fig. 13(c), and the corresponding slopes in Fig. 13(d). The latter profiles show a sharply peaked feature in the terrain near 62 nmi, with a total slope change of about 25°, which slightly exceeds the limit established in Section V. Therefore, to avoid errors, the propagation is calculated to a maximum range of about 62 nmi.

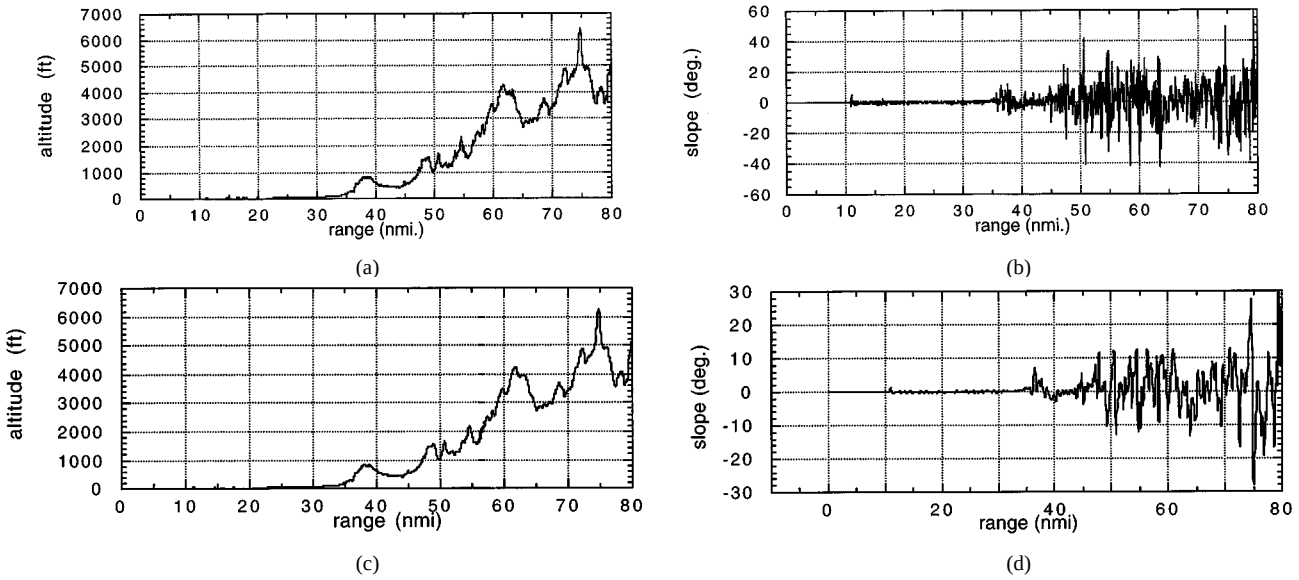

Fig. 13. (a) Sample terrain profile from the digital terrain elevation database (DTED) with (b) slope angles (β). (c) A filtered (smoothed) realization is shown with (d) corresponding slopes.

The impedance boundary condition for the shift map, developed in Section VI, requires knowledge of the grazing angle at each range step. For propagation over a terrain sample, the grazing angles are estimated numerically by the spectral estimation algorithm MUSIC. Details of the MUSIC implementation are described, for example, in [3] and [18]. The piecewise linear wide-angle shift map is first run over the terrain assuming perfect conductivity. This accounts for atmospheric refraction and gives a good approximation for the grazing angles on the boundary. The fields at each range step are then used to estimate the dominant propagation directions, which are stored for future use. The propagation is then recalculated using the new impedance boundary condition, with grazing angles taken from the perfectly conducting calculation. A similar approach has been used extensively for propagation over rough sea water [3] with excellent results.

Calculations are made from a source located 100 ft above the surface at $x = 0$ nmi. A 3-GHz antenna is directed at 0° elevation angle, with 3° main beamwidth. A complex dielectric constant with $\epsilon_1 = 80$ and $\sigma = 4$ mho/m is assumed everywhere, and standard atmosphere is used for the refractivity profile. Fig. 14 illustrates the result for vertical polarization. Substantial reflections from the terrain, and a complicated interference pattern, are observed. By comparing with the terrain profile [Fig. 13(c)] we find deep shadowing behind the various peaks in the terrain. Fig. 15 shows the same problem recalculated with the terrain masking approximation using exactly the same parameters as for Fig. 14, with the exception of surface conductivity, which requires to be infinite (Dirichlet boundary). By comparison, terrain masking substantially underestimates the shadowing, consistent with the results of Section VI.

The differences between terrain masking and the shift map approach over finitely conducting terrain are more clearly illustrated in Fig. 16. The various methods are compared at a fixed altitude of 100 ft above the terrain profile. Results are shown for a range of frequencies. In addition to the vertical polarized (Fig. 14) and terrain masking (Fig. 15) results, horizontal polarization and horizontal polarization/perfect conductor (sine transform, Dirichlet boundary) are also included in Fig. 16. Again, all problem parameters are the same, with the exception of surface conductivity (terrain masking) and boundary condition. At 500 MHz [Fig. 16(a)], it is found that H-polarized and V-polarized results are significantly different, particularly in the shadow zones. Especially noticeable are 20 dB or larger separations between H and V in the deep shadow regions (for example, 41, 49.5, 51–52, 55–56 nmi), in agreement with rough surface scattering theory that predicts much deeper shadows for H due to the effects of surface (creeping) waves at V. The H-polarized results over finite and perfect electrically conducting (PEC) surfaces are also substantially different. At a higher frequency of 3-GHz [Fig. 16(b)], the PEC and H-polarized results are indistinguishable. The shift map also predicts minor differences between H and V polarization, except perhaps in the deep shadow regions, where differences of several decibels are found. At much higher frequencies such as 10 GHz [Fig. 16(c)], as expected, all three shift map results converge. In general, we find that at S-band and higher frequencies, H polarization is relatively insensitive to surface conductivity. Vertical polarization becomes insensitive to conductivity at roughly X-band and higher. At much lower frequencies, both polarizations are strongly sensitive, which we have observed in calculations as low as 50 MHz. These polarization differences are also expected to be more significant for weakly conducting surfaces such as dry ground.

Finally, the results in Fig. 16 show that terrain masking, in comparison with the shift map, consistently overestimates the field in shadowed areas (the deeper the shadow, the greater the discrepancy). The terrain masking approach also significantly weakens surface reflections, as shown in Fig. 15. Although the Dirichlet boundary condition used suggests perfect conductivity (hence, perfectly reflecting), the reflections are lost by approximating the surface by a series of knife-edge diffractors. As a

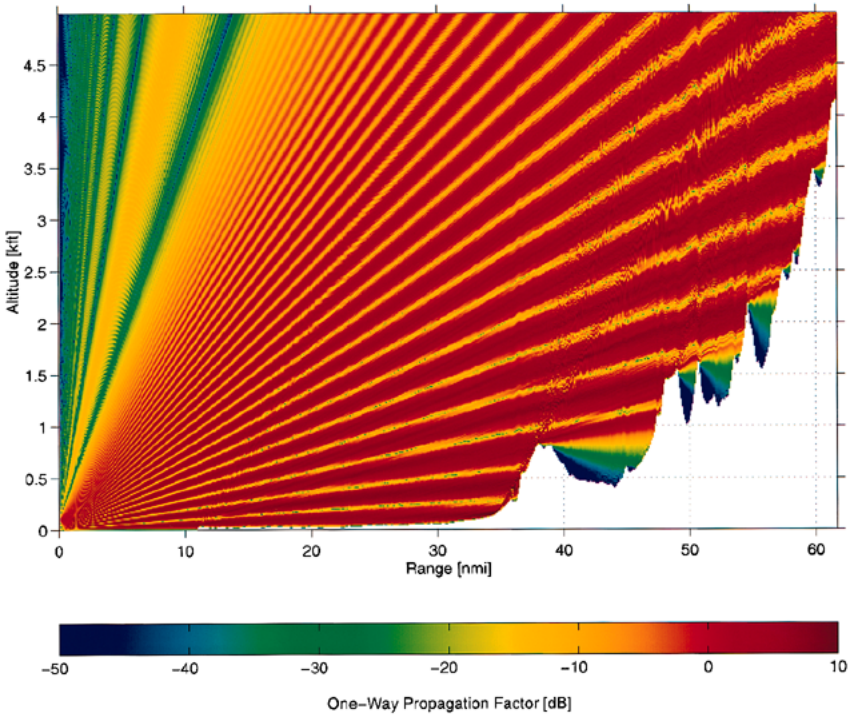

Fig. 14. Propagation over the terrain profile of Fig. 13(c) calculated by the piecewise linear wide-angle shift map with impedance boundary condition. A vertical polarized, 3-GHz source with 3° beamwidth is located 100 ft above the origin. Surface electrical parameters are $\epsilon_1 = 80$ and $\sigma = 4$ mho/m. Standard atmosphere is assumed.

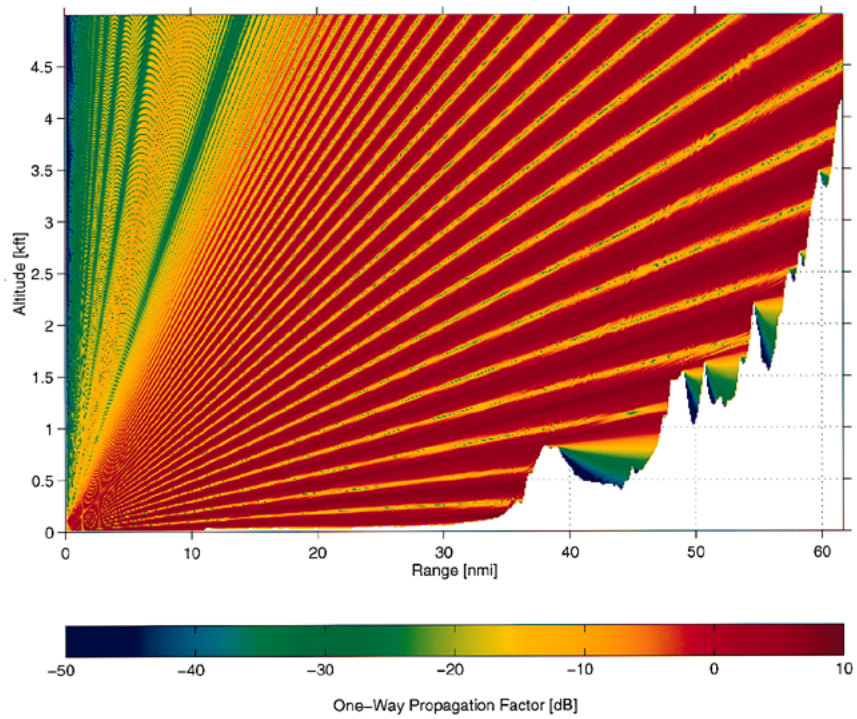

Fig. 15. Same as Fig. 14, but calculated by the terrain masking approximation (horizontal polarization, perfectly conducting).

result, the complicated multiwave interference pattern observed in Fig. 14 is not reproduced by terrain masking. Given the approximate nature of the terrain mask boundary condition and the good agreement shown earlier between shift map and GTD results, Fig. 16 suggests that terrain masking is a poor approximation, regardless of frequency.

IX. Summary

In the Fourier/split-step approach to numerically solving the PWE, several methods have previously been used for generating solutions over an undulating boundary, each with significant limitations. For example, all of the previous techniques are

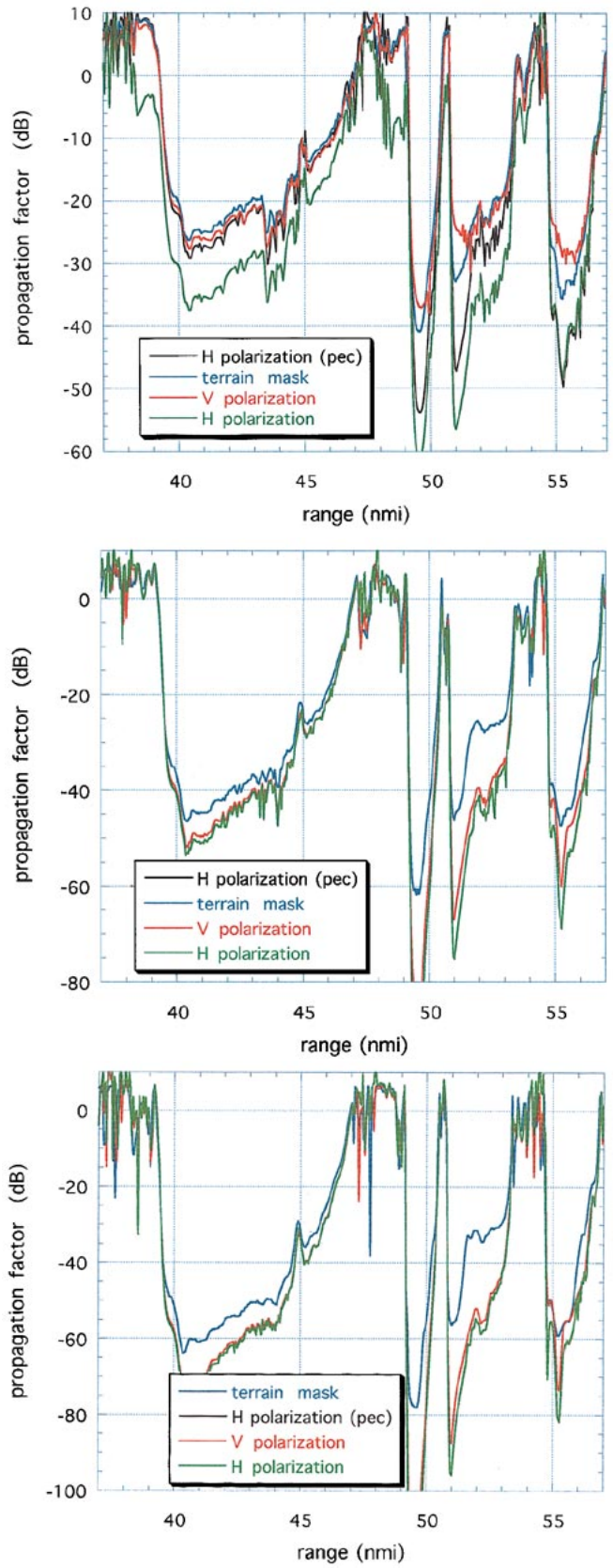

Fig. 16. Comparison of the relative intensity at 100 ft above the surface calculated by the terrain masking and shift map (horizontal polarization, vertical polarization, horizontal polarization over perfect conductor) methods, for the problem shown in Figs. 13–15. (a)–(c) 500 MHz, 3 GHz, and 10 GHz, respectively.

limited to perfectly conducting boundaries. A significant advance, the coordinate transformation technique of Beilis and Tappert [9], is derived from the paraxial approximation and is therefore restricted to narrow propagation angles about the horizon. The new methods developed in this paper, the shift map, extend the coordinate transformation technique to address these limitations. A wide angle form of the PWE is derived by starting from a coordinate transformation of the original Helmholtz equation, thereby avoiding the paraxial approximation. An extension of the Leontovich impedance boundary condition is also developed for the shift map that permits solution of the PWE over finitely conducting terrain using the previously developed mixed Fourier transform. The impedance boundary condition requires knowledge of the grazing angle on the boundary, which is also required for modeling the effects of fine-scale surface roughness.

The new shift map is extensively tested on both simple and more complex model terrain problems. For example, the numerical solutions are compared with GTD for the classical problem of diffraction by a perfectly conducting wedge. The more accurate piecewise linear form of the wide-angle shift map is found to be in excellent agreement with GTD, particularly in the deep shadow region behind the wedge. Propagation over a smoothly curved obstacle is also examined, and it is found that a piecewise linear representation of the shift map correctly approximates the continuous map, provided the curved terrain is adequately sampled. Interestingly, it is shown that the effect of surface curvature is accounted for in the piecewise linear representation by steering the field in discrete steps. The steering is analogous to that used in linear phased array antennas and is therefore physically intuitive.

Investigations of smoothly curved versus sharply peaked terrain features also show considerable differences in the shadowing or blockage of the low grazing angle field by the terrain. In the piecewise linear representation, strong tip diffraction can be modeled that significantly fills in the shadow regions. However, modeling such effects requires an accurate characterization of crested terrain. While diffraction by a rounded wedge can be modeled by other techniques, such as GTD, the PWE solution is valid at arbitrarily low frequency and may also include atmospheric refraction.

Through various investigations of triangular wedges (pyramids) and upward/downward sloping ramps, approximate slope limits are identified for the terrain. For example, noticeable errors are observed from a field incident at 20° grazing angle on a reflecting surface. A similar limit is observed for the total slope change between two successive linear terrain segments. When propagating over a 17.33° wedge, for example, a slight distortion of the field is observed in the entire vertical column above the wedge. At 25°, the solution clearly breaks down. The sources of these errors are clearly identified as a commutator error, split-step solution error and approximate expansion of the operator square root. By factoring the original Helmholtz equation in the physical coordinate system rather than the transformed coordinates, it is shown that the commutator error is minimized but cannot be eliminated for propagation at large angles from the horizontal. The square root expansion is also improved by the piecewise linear version of the shift map.

While the techniques presented in this paper have extended the accuracy of the split-step Fourier method to terrain with slopes as large as 20°, other approaches are required for terrain containing larger slopes. The approach we currently use, despite the limitations of the simple terrain mask approximation, is a hybrid scheme that alternates between piecewise linear shift map and terrain masking when steep slopes are encountered. However, because multiple surface reflections are poorly modeled by terrain masking, it is likely that multipath interference patterns are not well reproduced. This is confirmed by the extensive comparisons we have made between the two alternative methods. These comparisons also indicate that terrain masking consistently overestimates the field intensity in shadowed regions. A problem using digital terrain elevation data, for example, showed differences as large as 20 dB or greater for frequencies ranging from 500 MHz to 10 GHz. In general, the deeper the shadow, the greater the discrepancy between the two approaches. Such differences are of great interest to radar applications, where they impact the detectability of low-flying targets, and the clutter return from shadowed terrain.

In conclusion, we have demonstrated that the shift map approach significantly advances our ability to model practical terrain problems. While this represents an important new capability for propagation modeling, the examples demonstrate that the solution cannot accommodate all terrain scenarios of interest. To broaden the capability of the approach even further will require additional study. We wish to emphasize that there are many situations in which the usual approximations, such as perfectly conducting or rigid boundaries, horizontal polarization, and narrow angle propagation are inadequate and that a more general solution such as the one developed here must be employed.

ACKNOWLEDGMENT

The authors would like to thank G. D. Dockery for numerous discussions and insights.

REFERENCES

[1] S. Ramo, J. R. Whinnery, and T. Van Duzer, *Fields and Waves in Communication Electronics*. New York: Wiley, 1984.

[2] J. R. Kuttler and G. D. Dockery, "Theoretical description of the parabolic approximation/Fourier split-step method of representing electromagnetic propagation in the troposphere," *Radio Sci.*, vol. 26, pp. 381–393, 1991.

[3] G. D. Dockery and J. R. Kuttler, "An improved impedance boundary algorithm for Fourier split-step solutions of the parabolic wave equation," *IEEE Trans. Antennas Propagat.*, vol. 44, pp. 1592–1599, Mar./Apr. 1996.

[4] V. A. Fock, "Solution of the problem of propagation of electromagnetic waves along the earth's surface by method of parabolic equations," *J. Phys. USSR*, vol. 10, pp. 13–35, 1946.

[5] F. B. Jensen, W. A. Kuperman, M. B. Porter, and H. Schmidt, *Computational Ocean Acoustics*. New York: AIP, 1994.

[6] J. R. Kuttler and J. D. Huffaker, "Solving the parabolic wave equation with a rough surface boundary condition," *J. Acoust. Soc. Amer.*, vol. 94, pp. 2451–2454, 1993.

[7] S. Ayasli and M. B. Carlson, "SEKE: A computer model for low-altitude radar propagation over irregular terrain," MIT/Lincoln Lab. Project Rep., Cambridge, MA, CMT-70, 1985.

[8] L. B. Dozier, "PERUSE: A numerical treatment of rough surface scattering for the parabolic wave equation," *J. Acoust. Soc. Amer.*, vol. 75, pp. 1415–1432, 1984.

[9] A. Beilis and F. D. Tappert, "Coupled mode analysis of multiple rough surface scattering," *J. Acoust. Soc. Amer.*, vol. 66, pp. 811–826, 1979.

[10] D. J. Donohue, "Propagation modeling over terrain by coordinate transformation of the parabolic wave equation," in *Proc. 1996 IEEE Antennas Propagat. Int. Symp.*, Baltimore, MD, July 1996, p. 44.

[11] F. D. Tappert and L. Nghiem-Phu, "A new split-step Fourier algorithm for solving the parabolic wave equations with rough surface scattering," *J. Acoust. Soc. Amer. Suppl.*, vol. 77, p. S101, 1985.

[12] D. Rouseff and T. E. Ewart, "Effect of random sea surface and bottom roughness on propagation in shallow water," *J. Acoust. Soc. Amer.*, vol. 98, pp. 3397–3404, 1995.

[13] A. E. Barrios, "A terrain parabolic equation model for propagation in the troposphere," *IEEE Trans. Antennas Propagat.*, vol. 42, pp. 90–98, Jan. 1994.

[14] C. L. Rino and H. D. Ngo, "Forward propagation in a half-space with an irregular boundary," *IEEE Trans. Antennas Propagat.*, vol. 45, pp. 1340–1347, Sept. 1997.

[15] D. J. Thomson and N. R. Chapman, "A wide-angle split-step algorithm for the parabolic equation," *J. Acoust. Soc. Amer.*, vol. 74, pp. 1848–1854, 1983.

[16] D. J. Donohue and J. R. Kuttler, "Modeling radar propagation over terrain," *JHU/APL Tech. Dig.*, vol. 18, pp. 279–287, 1997.

[17] *Antenna Engineering Handbook*, R. C. Johnson and H. Jasik, Eds., McGraw-Hill, New York, 1984, pp. 19.6–19.7.

[18] M. H. Newkirk, "Recent advances in the tropospheric electromagnetic parabolic equation routine (TEMPER) propagation model," in *1997 Battlespace Atmosph. Conf.*, J. Richter, Ed. San Diego, CA: Office Dir. Defense Res. Engrg., SPAWAR, 1998.

[19] R. O. Schmidt, "Multiple emitter location and signal parameter estimation," *IEEE Trans. Antennas Propagat.*, vol. 34, pp. 276–280, Mar. 1986.

[20] D. A. McNamara, C. W. I. Pistorius, and J. A. G. Malherbe, *Introduction to the Uniform Geometrical Theory of Diffraction*. Norwood, MA: Artech House, 1990.

[21] C. A. Balanis, *Advanced Engineering Electromagnetics*. New York: Wiley, 1989.

[22] R. J. McArthur and D. H. O. Bebbington, "Diffraction over simple terrain obstacles by the method of parabolic equations," in *Inst. Elect. Eng. Proc. Int. Conf. Antennas Propagat.*, 1991, pp. 824–827.

[23] R. J. McArthur, "Propagation modeling over irregular terrain using the split-step parabolic equation method," in *Inst. Elect. Eng. Proc. Radar*, 1992, pp. 54–57.

[24] T. B. A. Senior and J. L. Volakis, *Approximate Boundary Conditions in Electromagnetics*. London, U.K.: IEE Press, 1995.

Denis J. Donohue (S'84–M'85) received the B.A. degree in computer science from Rutgers University, New Brunswick, NJ, and the Ph.D. degree in electrical engineering from Stanford University, Stanford, CA, in 1991.

Following a postdoctoral appointment working in space plasma physics, he joined the Research and Technology Development Center of the Johns Hopkins University Applied Physics Laboratory, Baltimore, MD, where he is currently a principal Staff Physicist. His research interests span a broad range in space science, optics, acoustics, electromagnetic theory and computational physics. He has concentrated for several years on radar propagation and scattering from the ocean surface and terrain.

Dr. Donohue is a member of the IEEE Antennas and Propagation Society and the U.S. National Committee of URSI (commision F).

J. R. Kuttler was born in Burlington, IA, in 1941. He received the B.A. degree in mathematics from Rice University, Houston, TX, in 1962, and the M.A. and Ph.D. degrees in applied mathematics from the University of Maryland, College Park, in 1964 and 1967, respectively.

Since 1967, he has been a Mathematician with the Johns Hopkins University Applied Physics Laboratory, Laurel, MD. He is presently a member of the Principal Professional Staff in the Radar Systems Department at that university. His areas of expertise are in partial differential equations, numerical analysis, finite differences, eigenvalue problems, Fourier analysis, signal processing, chemical phase transitions, synthetic aperture radar, electromagnetics, propagation, scattering and cross-section calculations, fractals, and fast convolution algorithms.